

# Simulation-Based Validation for Four-Dimensional Multi-Channel Ultrasound Current Source Density Imaging

Zhaohui Wang, *Member, IEEE*, and Russell S. Witte, *Member, IEEE*

**Abstract**—Ultrasound current source density imaging (UCSDI), which has application to the heart and brain, exploits the acoustoelectric (AE) effect and Ohm's law to detect and map an electrical current distribution. In this study, we describe 4-D UCSDI simulations of a dipole field for comparison and validation with bench-top experiments. The simulations consider the properties of the ultrasound pulse as it passes through a conductive medium, the electric field of the injected dipole, and the lead field of the detectors. In the simulation, the lead fields of detectors and electric field of the dipole were calculated by the finite element (FE) method, and the convolution and correlation in the computation of the detected AE voltage signal were accelerated using 3-D fast Fourier transforms. In the bench-top experiment, an electric dipole was produced in a bath of 0.9% NaCl solution containing two electrodes, which injected an ac pulse (200 Hz, 3 cycles) ranging from 0 to 140 mA. Stimulating and recording electrodes were placed in a custom electrode chamber made on a rapid prototype printer. Each electrode could be positioned anywhere on an  $x$ - $y$  grid (5 mm spacing) and individually adjusted in the depth direction for precise control of the geometry of the current sources and detecting electrodes. A 1-MHz ultrasound beam was pulsed and focused through a plastic film to modulate the current distribution inside the saline-filled tank. AE signals were simultaneously detected at a sampling frequency of 15 MHz on multiple recording electrodes. A single recording electrode is sufficient to form volume images of the current flow and electric potentials. The AE potential is sensitive to the distance from the dipole, but is less sensitive to the angle between the detector and the dipole. Multi-channel UCSDI potentially improves 4-D mapping of bioelectric sources in the body at high spatial resolution, which is especially important for diagnosing and guiding treatment of cardiac and neurologic disorders, including arrhythmia and epilepsy.

## I. INTRODUCTION

ELECTRICAL mapping is a common procedure during treatment of a serious arrhythmia in the heart or recurrent seizures in the brain. Much effort and many techniques have been applied to improve the mapping performance, including spatial resolution and accuracy. Elec-

troencephalography (EEG) and magnetoencephalography (MEG), for example, are popular, noninvasive and safe techniques that explore the location of brain source activity by using an inverse solution; the electrocorticogram (ECoG) [1] has better SNR and temporal and spatial resolution than EEG because the ECoG signals are recorded in the area of the underlying brain sources without the influence of the low conductivity of the skull. Because the recorded signal is the spatial summation of the impressed current densities induced by the highly synchronized post-synaptic potential occurring in large clusters of neurons, and a typical cluster size must cover at least 40 to 200 mm<sup>2</sup> of cortical surface, these methods (EEG, MEG, and ECoG) based on the inverse solution are ambiguous in localizing a source arising from deep below the surface. The electrical signal is often assumed to be close to the surface of the brain or heart [2], and a statistical  $t$ -statistic is typically used to determine activation [3].

On the other hand, ultrasound current source density imaging (UCSDI) [4]–[6], based on the acoustoelectric (AE) effect, an interaction between pressure and resistivity, potentially overcomes limitations of conventional electrophysiology by providing spatial information that is confined to the ultrasound focus, leading to more remote detection schemes. In UCSDI, an ultrasound pulse is focused on the tissue (e.g., nerve bundle) with a lateral spatial resolution ( $\approx 1.22\lambda$ -f-number) determined by the acoustic wavelength  $\lambda$  (e.g., 1.5 mm at 1 MHz) and f-number of the transducer. The axial resolution (along the depth direction) for UCSDI is determined by the length of the ultrasound wave packet. UCSDI can also be combined with pulse-echo (PE) ultrasound as an anatomical reference by detecting the echo of the same transmitted ultrasound pulse. Thus, electrical and anatomical information can be merged into a single image. EEG/ECoG-based current density reconstruction (CDR) instead relies on a subject's magnetic resonance (MR) or computed tomography (CT) image data as an anatomical reference, and an FEM model based on MRI data cannot typically be made at the time of treatment [1].

In the AE effect, the ultrasound pulse applies pressure to modulate the moving charges in the conductive media, and the detected AE signal is proportional to the applied pressure and current density and sensitive to the direction of current flow [7], [8]. AE tomography [9] described the electric impedance properties of biological tissue with high spatial resolution, and the contrast was related to the electric impedance, modulation coefficient, and acoustic

Manuscript received August 3, 2013; accepted December 16, 2013. This work was supported by grants from the National Institutes of Health (NIH; R01EB009353), the Technology and Research Initiative Fund (TRIF), and the Advanced Research Institute for Biomedical Imaging (ARIBI).

Z. Wang is with the Electrical and Computer Engineering Department, University of Arizona, Tucson, AZ, and the Heart and Vascular Institute, University of Pittsburgh Medical Center, Pittsburgh, PA (e-mail: wangzh@ustc.edu).

R. S. Witte is with the University of Arizona, Tucson, AZ (e-mail: rwitte@email.arizona.edu).

DOI <http://dx.doi.org/10.1109/TUFFC.2014.2927>

properties of the tissue. UCSDI was used to map cardiac activation waves in the live rabbit heart, with measured conduction velocities estimated from the images to be on the order of 0.12 mm/ms [10], [11]. Its sensitivity is proportional to the amplitude and geometry of the local current density and pressure at the focus [7], [8], [12]. Unipolar ultrasound pulses have also been used in simulation to reconstruct arbitrary current distributions in a conductive volume [13]. In the previous work of a 2-D dipole field [14], [15], UCSDI was tested under controlled conditions and compared with conventional electrical mapping techniques, but it failed to demonstrate how to capture the orientation and polarity of a volume dipole field.

Multichannel burst-mode acquisition in the electrode chamber forms high-quality four-dimensional current density images in spatial and temporal domains. It not only detects the polarity and amplitude of current density, but also tracks its change over time. As the ultrasound pulse passes through the conductive medium, it convolves/correlates with the inner product of the electric field of the dipole and the lead field of the detector, making the shifting frequency for polarity lower than the center frequency of the ultrasound pulse. After the AE signal is shifted to baseband, the AE voltage is positive at the anode and negative at the cathode. Real-time volumetric imaging of current flow (UCSDI) simultaneously co-registered with anatomy (standard ultrasound) and conventional electrophysiology [e.g., electrocardiography (ECG) or EEG] potentially facilitates corrective procedures for cardiac and neural abnormalities. This study reviews the theory of UCSDI and carries out simulations and bench-top experiments to analyze the performance of this novel imaging technique.

## II. METHODS

### A. 4-D Acoustoelectric Equation and Theory

UCSDI is based on the AE effect and reciprocal theory [6]. Fig. 1 illustrates the concept of the AE effect in connection with the experiments described in this paper. Current injected between two electrodes in a conductive medium produces an electrical dipole, and a focused ultrasound transducer is used to modulate the resistivity near the focus [see Fig. 1(a)]. Fig. 1(b) depicts an injected current with a waveform similar to a physiologic signal (like an ECG or local field potential) following physiologic time  $t_s$ , while the ultrasound transducer is excited at a pulse repetition frequency (PRF) of 2.5 KHz.

As ultrasound propagates through a uniform conducting media, the voltage signal  $V_i^{\text{AE}}$  can be detected using recording electrodes [Fig. 2(a)] according to Ohm's law and the AE effect. In Fig. 1(a), the dipole coordinate system and transducer coordinate system are used to describe the electric field, lead field, and acoustic pressure field. The center of the transducer is focused at  $D(x_0, y_0, z_0)$  in the dipole coordinate system (the origin is at the center

of the rectangular bath). In the electric field, because of a distributed current source  $\mathbf{J}^{\text{I}} = \mathbf{J}^{\text{I}}(x, y, z, t_s)$ , the voltage  $V_i^{\text{AE}}$  measured by lead  $i$  at coordinates  $x_0, y_0, z_0$ , and time  $t_s$  can be expressed in four dimensions under the assumption of far-field detection of the AE signal. To reduce the noise interference, a band-pass filter  $h(t)$  with a center frequency similar to the transducer is applied to the AE signal  $V_i^{\text{AE}}$  [6], [12]. In the simulations and experiment, the transducer is steered along the  $x$ - $y$  plane, and the dipole is near the focus of the transducer; therefore,  $z_0$  is constant and  $z_0 = -z_f$  (the focal length of the transducer). Any point  $P$  in the ultrasound pressure field  $(x, y, z)$  can be described in the dipole coordinate system as  $(x + x_0, y + y_0, z + z_0)$ , or  $\overline{DP} = \overline{DT} + \overline{TP}$ . The ultrasound beam pattern and pulse waveform were also introduced to describe the AE signal using [6], [15]

$$V_i^{\text{AE}}(x_0, y_0, t, t_s) = -P_0 \iiint K_1 \rho_0 \mathbf{J}_i^{\text{L}}(x + x_0, y + y_0, z + z_0) \cdot \mathbf{J}^{\text{I}}(x + x_0, y + y_0, z + z_0, t_s) \cdot \left[ b(x, y, z) a\left(t - \frac{z}{c}\right) \right] dx dy dz, \quad (1)$$

where  $P_0$  is the amplitude of the pressure pulse;  $K_1$  is the interaction constant, whose value is on the order of  $10^{-9} \text{ Pa}^{-1}$  in saline [5];  $\rho_0$  is direct current resistivity;  $\mathbf{J}_i^{\text{L}}(x, y, z)$  is the electric lead field resulting from the unit reciprocal current formed by the detector  $i$ ;  $b(x, y, z)$  is the ultrasound beam pattern defined with respect to the transducer;  $a(t - z/c)$  is the pulse waveform;  $c$  is the speed of sound;  $t$  is the ultrasound fast time; and  $t_s$  is the physiologic slow time, with  $t_s = t + mT$ , where  $T = 1/\text{PRF}$  and  $m$  is the integer number of bursts.

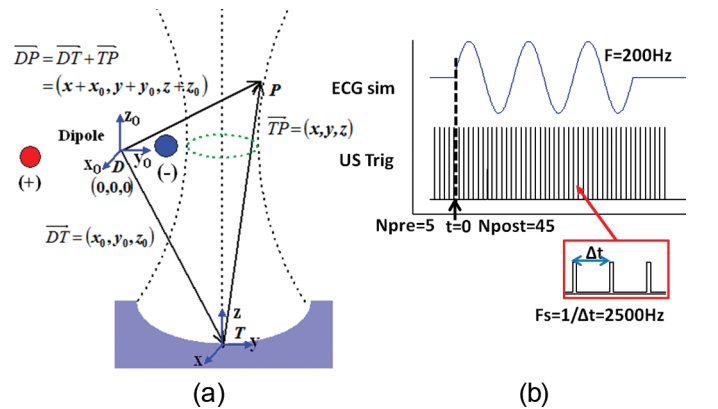


Fig. 1. (a) Schematic illustration of the AE effect that comes from the correlation between the ultrasound pulse and the inner product of the electric field of the dipole and lead field of the detector.  $D(0, 0, 0)$  is the origin of the coordinate system of the electric field. Transducer center is at  $T(x_0, y_0, z_0)$ , and any point  $P$  in the ultrasound pressure field  $(x, y, z)$  can be described in the electric field as  $(x + x_0, y + y_0, z + z_0)$ , or  $\overline{DP} = \overline{DT} + \overline{TP}$ . (b) The injected current was a 200-Hz sine wave burst; the ultrasound transducer was excited at 2.5 kHz. The acquisition time period was 20 ms, and the first ultrasound pulse occurred 2 ms before the current burst.

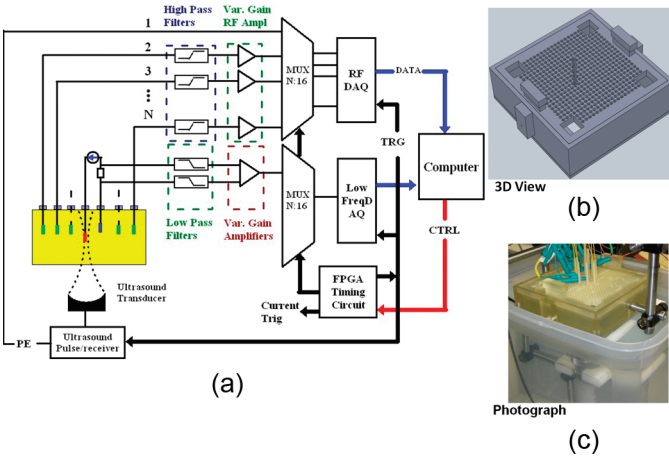


Fig. 2. Apparatus for 4-D multichannel UCSDI. (a) Ultrasound transducer was steered in the  $x$ - $y$  plane with a step of 0.5 mm, sending out pulses from the bottom of the chamber. Low-frequency current was injected from a function generator controlled by a timing circuit, and the electric field between the platinum electrodes formed a dipole. The AE signals were detected by the recording Ag/AgCl electrodes, filtered by a high-pass filter, amplified, and sampled by the high-frequency channels, which were synchronized with the pulse/receiver in burst mode [Fig. 1(b)]. The injected current was sampled by a low-frequency channel. (b) Custom chamber for the experiment created in SolidWorks. (c) Photograph of chamber fabricated on a 3-D printer with electrodes in position and transducer below.

Because  $K_I = K_I(x, y, z)$  and  $\rho_0 = \rho_0(x, y, z)$  both depend on the material properties, they can be combined together with  $\mathbf{J}_i^L$  and  $\mathbf{J}^I$ , so that

$$w_i(x, y, z, t_s) = K_I(x, y, z)\rho_0(x, y, z)\mathbf{J}_i^L(x, y, z) \cdot \mathbf{J}^I(x, y, z, t_s). \quad (2)$$

The ultrasound wave field is simulated using Field II software [12], and the pulse can be simplified by

$$p(x, y, z, t) = P_0 b(x, y, z) a(t - z/c). \quad (3)$$

$V_i^{AE}(x_0, y_0, t, t_s)$  involves three correlations of  $w(x, y, z, t_s)$  and  $p(x, y, z, t)$ , so its computation can be accelerated by the 3-D Fourier transform.

$$\begin{aligned} V_i^{AE}(x_0, y_0, t, t_s) &= -\iiint w_i(x + x_0, y + y_0, z + z_0, t_s) \\ &\quad \cdot p(x, y, z, t) dx dy dz \\ &= -F_{x_0, y_0, z_0}^{-1} \{W_i(k_x, k_y, k_z, t_s) \\ &\quad \cdot F_{k_x, k_y, k_z}^* [p(x, y, z, t)]\}, \end{aligned} \quad (4)$$

where  $z_0 = -z_t$ ,  $F_{x_0, y_0, z_0}^{-1}$  is the 3-D inverse Fourier transform over  $(k_x, k_y, k_z)$ ,  $W$  is the 3-D Fourier transform of  $w(x, y, z)$ ,  $F_{k_x, k_y, k_z}$  is the 3-D Fourier transform over  $(x, y, z)$ , and  $F_{k_x, k_y, k_z}^*$  is the conjugate of  $F_{k_x, k_y, k_z}$  over  $k_x$ ,  $k_y$ , and  $k_z$ .

The current density  $\mathbf{J}^I$  of the dipole is modeled as the gradient of the dipole potential  $V^I$ ,

$$\mathbf{J}^I(x, y, z, t_s) = -\sigma_i \nabla V^I(x, y, z, t_s), \quad (5)$$

where  $\nabla$  is the gradient operator and  $\sigma_i$  is the local conductivity.

In the saline solution, the transmitted ultrasound pulse correlates with the inner product of the lead fields, potentially shifting the spectrum of the AE signal  $V_i^{AE}$  to a slightly lower frequency. The polarity and envelope of the AE voltage  $V_i$  can be extracted together after shifting the AE signal to baseband [8]. The lead field of detector  $i$  can further be expressed as the gradient of the lead field potential  $V_i^L$ ,

$$\mathbf{J}_i^L(x, y, z) = -\sigma_i \nabla V_i^L(x, y, z), \quad (6)$$

and the AE voltage can be described by the inner product of the gradient of potentials in the dipole electric field and lead field of detector  $i$ .

$$\begin{aligned} V_i(x, y, z, t_s) &\approx -P_0 K_I \rho_0 \mathbf{J}_i^L(x, y, z) \cdot \mathbf{J}^I(x, y, z, t_s) \\ &= -P_0 K_I \sigma_i \nabla V_i^L \cdot \nabla V^I. \end{aligned} \quad (7)$$

Therefore, the polarity of the dipole ( $V^I$ ) can be determined from the detected AE voltage and lead fields formed by the detectors [6].  $V^I$  can be approximated by the AE voltage  $V_i$  by shifting the AE signal  $V_i^{AE}$  to baseband or the averaged AE voltage  $V$  for multiple channels.

The current source is the divergence of current density, or the Laplacian of the AE voltage  $V_i$  (or the averaged AE voltage  $V$  for multiple channels):

$$I_{CSD}(x, y, z, t_s) = -\nabla \cdot \mathbf{J}^I(x, y, z, t_s) \approx \sigma_i \Delta V_i(x, y, z, t_s). \quad (8)$$

### B. UCSDI Experimental Setup

A time-varying 3-D dipole field was produced in a bath of 0.9% NaCl solution with a current ranging from 0 to 140 mA between the exciting dipole. A 1-MHz ultrasound beam was pulsed and focused through a plastic film attached to the bottom of a custom tank to modulate the current distribution. A 2-D raster scan of the transducer from the bottom of the saline chamber provided a 3-D image (scan spacing = 0.5 mm). The lateral resolution of UCSDI is determined by the size of the focal spot of the 1-MHz ultrasound transducer (f-number = 1.78), given by  $1.22\lambda \cdot \text{f-number} = 3.2$  mm.

The electrode chamber [Fig. 2(b)] can hold more than 400 electrodes for controlled experiments in saline. The chamber was designed in SolidWorks (Dassault Systèmes SolidWorks Corp., Waltham, MA) and fabricated on a 3-D rapid prototype printer (Objet350 Connex, Stratasys Ltd., Edina, MN). Each electrode can be placed anywhere on an  $x$ - $y$  grid (5 mm spacing) and individually adjusted in the depth direction for precise alignment of the stimulating and recording electrodes (cylinders with radius of 0.15 mm and length of 3 mm). A  $40 \times 40$  mm square window of Mylar film (TAP Plastics Corp., San Leandro, CA) was attached to the bottom of the chamber. The

ultrasound beam was steered mechanically through this window.

The multichannel data acquisition system [NI PXI-5105, National Instruments Corp., Austin, TX; see Fig. 2(a)] acquired data at 15 MHz up to 16 channels simultaneously [up to 6 were used in this study, Fig. 2(c)]. One NI PXI-6289 board was used for low-frequency channels to acquire current data at a sampling frequency of 20 kHz, and the other NI PXI-6289 board was used to control the timing of the ultrasound and current triggers. The acquired time period was 20 ms, and the first ultrasound pulse started 2 ms before the current injection [Fig. 1(b)]. A pulse/receiver (5077PR, Olympus NDT Inc., Waltham, MA) excited a single-element focused transducer (1 MHz,  $f$ -number = 1.78, focal length 68 mm) at a repetition rate of 2500 Hz. Pulse echo signals were also acquired by the transducer, providing dual-modality ultrasound and UCSDI. In Fig. 2(a), one pair of stimulating platinum electrodes were separated by 5 mm and used to inject a current burst (3 cycles at 200 Hz) into the saline solution. The Ag/AgCl recording electrodes were arranged with different configurations near the dipole for detecting the AE signal. The cathode of the dipole was used as a ground reference. The injected current was also measured across a 1- $\Omega$  resistor, amplified and low-pass filtered by a differential amplifier, and captured by an acquisition board (NI PXI-6289, National Instruments Corp.). The recording electrodes were connected to differential amplifiers (1855DA, LeCroy Corp., Chestnut Ridge, NY) for detecting the AE signals at different positions, and these AE signals were further amplified (AU-2A-0110, MITEQ Inc., Hauppauge, NY), low-pass filtered (BLP-5, MiniCircuits, Brooklyn, NY), and captured by a fast acquisition board (NI PXI-5105, National Instruments Corp.). The total amplification of the AE signals was 56 dB.

Two experiments were designed to measure the dimensions of the dipole, sensitivity/SNR, and the effect of recording distance or angle to the dipole. In the first experiment [Figs. 3(a)–3(c)], the orientation of the dipole in the  $x$ - $z$  plane was  $0^\circ$ , and the recording electrodes were 5 mm away and lined up horizontally with the center of the dipole. In the second experiment [Figs. 3(d)–3(f)], the orientation of the dipole in the  $x$ - $y$  plane was  $44.2^\circ$ , and the electrodes were arranged in a circle with approximately equal distances to the dipole. Color M-mode images of a time-varying dipole can be used to reconstruct the current waveform, assess sensitivity for detecting current injections, and examine effect of electrode distance on SNR.

### C. Data Processing

The acquired high-frequency data are five-dimensional: A-line sample points  $\times$   $x$ -position  $\times$   $y$ -position  $\times$  ultrasound trigger  $\times$  current trigger. In these experiments, 2048 points were captured at a sampling frequency of 15 MHz. Twenty current triggers were averaged at each position. The raw data were first filtered by a slow time band-pass filter centered at 200 Hz for each channel and each  $x$ - $y$

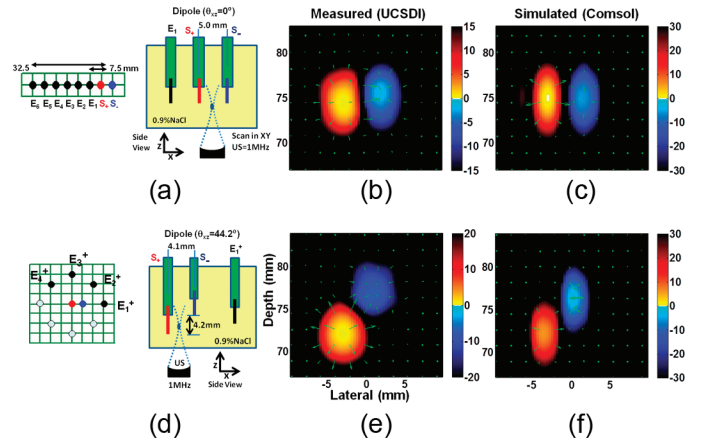


Fig. 3. Comparison of AE voltages reconstructed from the simulation and experiment for two dipole configurations. (a)–(c) Color B-mode UCSDI recorded on a single electrode  $E_1$  for dipole with  $0^\circ$  inclination. The two injecting electrodes are both at the same depth, about 75 mm. Current direction and magnitude are plotted on the 2-D image of  $V$  along the lateral-depth plane through the center. The image is displayed in a hot–cold decibel colormap with dynamic range  $[-15, 15]$  dB for the measured data and  $[-30, 30]$  dB for the simulated. (d)–(f) Color B-mode UCSDI recorded on a single electrode  $E_1^+$  for dipole with  $44.2^\circ$  inclination. The two injecting electrodes are at different depths; one is at 72 mm and the other at 76 mm. Current direction and magnitude are plotted on the 2-D image of  $V$  along the lateral-depth plane through the center. The image is displayed in a hot–cold decibel colormap with dynamic range  $[-20, 20]$  dB for the measured data and  $[-30, 30]$  dB for the simulated.

position. The AE signal was band-pass filtered at 1 MHz to remove out-of-band noise. The gradient of the UCSDI map was taken to provide the direction and magnitude of the current density, while the divergence was performed to obtain an image of the current source and sink.

As the AE signal was generated by the correlation between the 1 MHz ultrasound pulse and the current distribution, the center frequency of the detected AE signal may be slightly lower than the 1 MHz center frequency of the transducer. The AE spectrum was shifted to baseband to demodulate the high-frequency signal and determine the sign (polarity) of the current injection. Following the phase of the current injection at each depth, the phase along slow time synchronizes with the injected current. The magnitude (envelope) of the AE signal follows the phase and amplitude of the current injection at each depth.

The reconstructed dipole polarity of different channels must be synchronized with the injected current by using one marked position at the maximal absolute AE voltage. Each channel must be adjusted according to this reference position. The total volume (3-D) or area (2-D) of anodes and cathodes was maximized to optimize the shift frequency, rendering the cathode and anode on the images large and uniform. In Fig. 3(b), the area of dipole is about  $36.9 \text{ mm}^2$  for the anode and  $29 \text{ mm}^2$  for the cathode.

### D. UCSDI Simulation

Following (1), the simulated AE signal can be obtained after the lead field of the detector and electric field of the

dipole are applied with inner product and correlated with the ultrasound field. In the simulation, the spatial arrangement of the electrodes is consistent with the experiments [Figs. 3(a) and 3(d)]. The lead fields  $\mathbf{J}_i^L$  and electric field  $\mathbf{J}^I$  must be simulated according to the superposition principle ([16]) using the Comsol 3-D conductive media dc model (Comsol Inc., Burlington, MA), in which the anode of the dipole and each detecting electrode are individually assumed to be voltage sources [17]. For the electric field of the dipole ( $\mathbf{J}^I$ ), one of the dipole electrodes is set for positive potential, and the other electrodes are connected to ground; for the lead field of the detector ( $\mathbf{J}_i^L$ ), the detector is assumed to have a positive potential with unit reciprocal current, and the other electrodes are connected to the ground. In the experiment, the ultrasound pulse interacts with the current mostly from the bottom surface of the injecting electrodes, shifting the spectrum lower and working as a low-pass filter [4], so the effective length of the electrode in the simulation is less than the actual value of 3 mm. In the simulation, the injecting electrodes are set as ellipsoids with half-lengths along  $x$  and  $y$  of 0.15 mm, and  $z$  of 0.1 mm.

The ultrasound pulse waveform was extracted from one A-line acquisition using a commercial hydrophone (HDL-200, Onda Corp., Sunnyvale, CA) that detects the AE signal, while the PE signal was received by the pulse/receiver and sampled by the National Instruments system. Before simulating the AE signal according to (1), the PE pulse waveform was smoothed by a Hanning filter. The Field II software was used to build the pressure field  $p(x, y, z, t)$ . The calculation of multi-dimensional correlation/convolution is time-consuming, so forward and inverse Fourier transforms were used to speed up the 3-D correlation [see (4)].

### III. RESULTS

The region-of-interest (ROI) is the area in depth from 67 mm to 80 mm near the focus. Images are displayed in a decibel scale using a hot-cold decibel color map. The positive potential is displayed in red; the negative in blue. SNR is defined as the ratio of the peak value at the marked position to that in the selected background region in decibels.

#### A. Color 4-D UCSDI

4-D UCSDI of a time-varying dipole can be captured with as few as one detector and ground. A scan of the ultrasound transducer produces 2-D and 3-D spatial images of the current densities. These images can further be used to determine the location of the current source and sink. The color B-mode UCSDI in Fig. 3 shows the  $x$ - $z$  plane at  $y = 0$ . The full-width at half-maximum (FWHM) of the reconstructed current dipole determined from the divergence of the current source density image is 3.9 mm ( $x$  and  $y$ ) and 4.9 mm (along  $z$ , or depth). At  $i = 140$  mA,

the decibel value of the AE signal along fast time contains high SNR ( $>20$  dB), and also more than 20 dB along slow time, so the total SNR for M-mode color imaging is more than 40 dB. The 4-D color UCSDI movie reveals the amplitude and phase of the time-varying waveform at each pixel in the volume image with a temporal resolution of 400  $\mu$ s. The UCSDI images can be superimposed on the PE signal (gray scale), which was collected simultaneously, confirming the position of the electrodes. Fig. 4(a) (with supplementary movie [18]) shows a 4-D coregistered image of the PE ultrasound data and the AE voltage that alternates with the time-varying current.

#### B. Comparison With Simulation

In Fig. 5, the simulation of detector  $E_2^+$  is chosen for illustration, as each detector can achieve similar results. After correlations are done with Fourier transforms, the simulated AE signal was shifted to baseband to extract the polarity and envelope of the current density. At the anode, the gradient of  $V_2^L$  [Fig. 5(b)] is opposite to the gradient of  $V^I$  [Fig. 5(a)], then the value of  $V_2$  becomes positive [see Fig. 5(d)]; at the cathode, both gradients are in the same direction, then  $V_2$  is negative. Therefore, the AE effect can record the polarity of the dipole electric field. Fig. 5(d) shows that the AE voltage can be used to approximate the polarity of the dipole [Fig. 5(a)].

In Fig. 3, the reconstructed AE voltage rebuilt from the simulated AE signal is close to the experimental data. If no correlation from the ultrasound pulse is applied, the inner product of the dipole electric field and detector lead field has a large dynamic range of  $[-80, 80]$  dB (second row of Fig. 6). However, if the correlation with the ultrasound pulse is applied, the simulated AE voltage ( $V$ ) and current source ( $\Delta V$ ) are in a smaller range,  $[-30, 30]$  dB (see Fig. 6 for dipole at  $0^\circ$ ). In Fig. 4(b), the 3-D AE voltage reconstructed from the simulated AE signals with

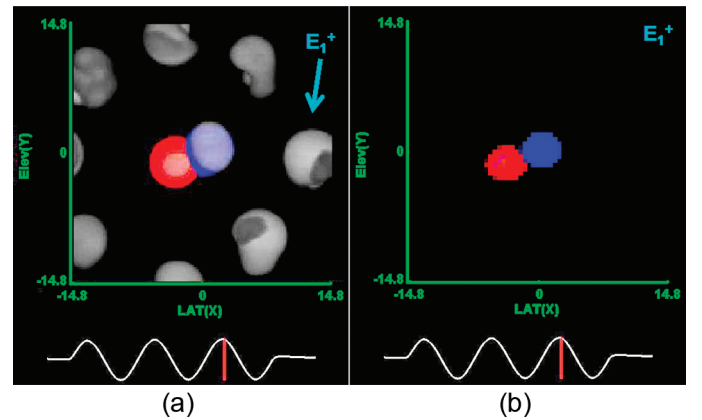


Fig. 4. Top view of (a) 3-D UCSDI (color) and pulse echo (gray) and (b) 3-D UCSDI simulation reconstructed from AE signals detected by the recording electrode on the right ( $E_1^+$ ). (a) The AE data are coregistered with the PE signal, which provided structural information. (b) 3-D AE voltage reconstructed from simulated AE signals shown at peak injected current. Colormap range is  $[-20, 20]$  dB for the experimental AE voltage  $[-20, 0]$ , for PE data, and  $[-30, 30]$  dB for the simulated AE voltage.

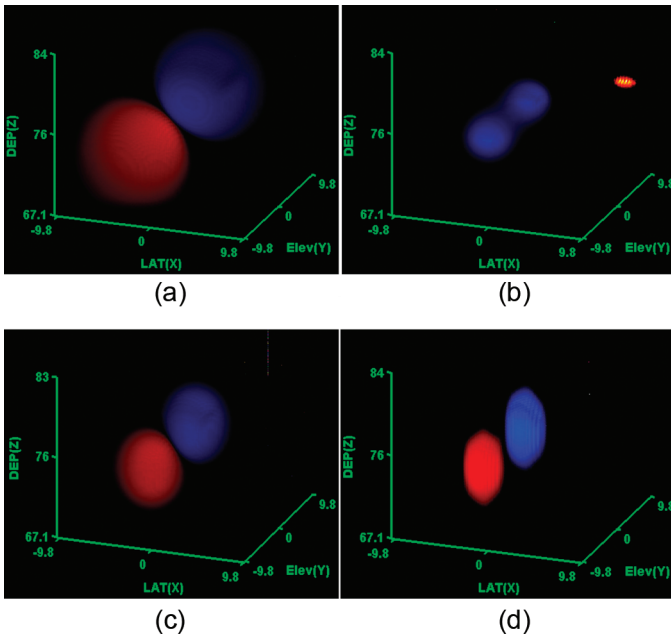


Fig. 5. Simulated AE signal obtained by the detector  $E_2^\dagger$  that is arranged on the circle around the dipole [Fig. 3(d)]. (a) The electric potential  $V^l$  of the lead field created by the dipole with inclination angle of  $44.2^\circ$ . (b) The electric potential  $V_2^l$  of the lead field created by the detector  $E_2^\dagger$  and ground. (c) The result of  $-\mathbf{J}_i^l \cdot \mathbf{J}^l$ , the inner product between the current densities of the lead fields created by detector  $E_2^\dagger$  and the dipole. (d) The AE voltage  $V_2$  after shifting the spectrum of the correlation between  $-\mathbf{J}_i^l \cdot \mathbf{J}^l$  and the ultrasound pulse to baseband. The images are displayed in a hot-cold decibel colormap with dynamic range  $[-30, 30]$  dB for (a) and (d),  $[-7, 7]$  dB for (b), and  $[-80, 80]$  dB for (c).

maximal injected current compares well with the measured 4-D UCSDI images.

In the case of electrodes at the same depth, the center frequency of the AE signal was 0.82 MHz for the simulation, and 0.88 MHz for the experimental data, whereas in the case of different depths, the center frequency was 0.8 MHz for the simulation, and 0.94 MHz for the experimental data. In Fig. 6(a), the volume of the measured dipole is about  $183 \text{ mm}^3$  for the anode and  $111.6 \text{ mm}^3$  for the cathode.

### C. Distance Effect

Six electrodes were arranged with a distance from the center of the dipole of 7.5, 12.5, 17.5, 22.5, 27.5, and 32.5 mm [Fig. 7(a)]. The detected phases at the marked position were 1.9776,  $-1.0288$ ,  $-0.2912$ ,  $-0.1281$ , 0.374, and 2.164 rad. In Fig. 7(a), the polar plot shows that phase extends as a helix with increased distance, whereas in the simulation, the phase changed only within a narrow range: 3.11, 3.09, 3.09, 3.1, 3.1, and 3.12 rad. Therefore, UCSDI is sensitive to the distance from recording electrode to the dipole, and the phase of the detectors on the edge deviates more than the inner detectors; however, this distortion can be corrected by synchronizing the phase of the marked position with the injected current [Fig. 7(b)].

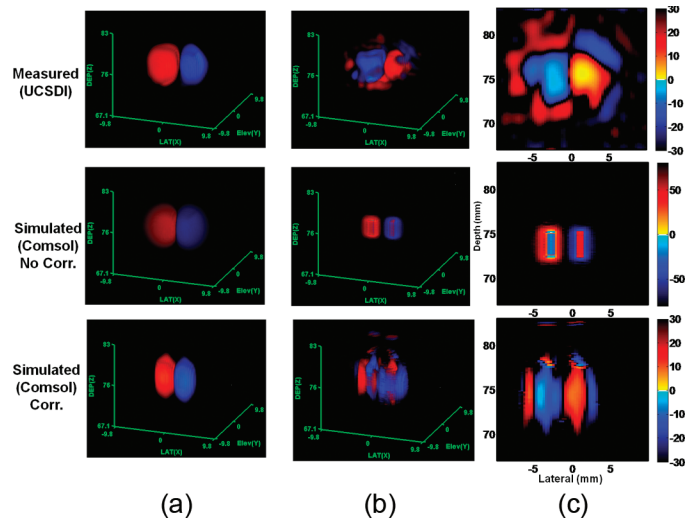


Fig. 6. Comparison between measured (UCSDI) and modeled (with and without correlation) images of current dipole with zero inclination angle in saline. (a) UCSDI in volts; (b) current source from Laplacian of (a); and (c) the lateral-axial plane through the center of Laplacian image denoting current source and sink. The injecting electrodes are at  $z = 75 \text{ mm}$ . Dynamic range is  $[-30, 30]$  dB for measured data,  $[-80, 80]$  dB for simulated data without correlation, and  $[-30, 30]$  dB for the simulated result with correlation.

The performance of the reconstructed data can be improved by averaging over multiple recording electrodes. To calculate SNR, the value at the marked position is defined as the signal, whereas the peak value in the left-bottom region is selected as the noise. In Fig. 7(c), the SNRs of the six channels are, respectively, 29.1, 29.08, 26.5, 27.5, 25.7, and 24 dB, whereas the SNR of the averaged data are approximately 29 dB; therefore, the SNR and sensitivity decay with distance from the dipole.

### D. Angle Effect

Eight detectors were arranged around the dipole with the distance from the detector to the dipole constant. The angle between the detector and the dipole increased from  $0^\circ$  to  $135^\circ$  with an interval of  $45^\circ$ . Channels 1–4 were connected to the positive inputs of the differential amplifiers with the negative inputs connected to the ground, and channels 5–8 were connected to the negative inputs of the differential amplifiers with the positive input connected to the ground. The maximal value of channels 1–4 lies in the fourth channel [Fig. 8(a)], and its position was marked as the reference position to synchronize all other channels. The reconstructed 4-D images from these channels were coregistered using this marked position [Fig. 8(b)]. Both phase and amplitude at the marked position deviated in small range. The amplitude and phase of measured data at the marked position were individually (amplitude in any unit/phase in radians)  $20 \angle -0.1689$ ,  $19.8 \angle 0.0096$ ,  $21.1 \angle 0.0891$ ,  $24.7 \angle 0.0702$  for channels 1–4, and  $17.8 \angle -0.11$ ,  $18.7 \angle 0.141$ ,  $18.3 \angle -0.16$ ,  $15.9 \angle 0.128$  for channels 5–8 [red circles in Fig. 8(a)]; whereas the amplitude and

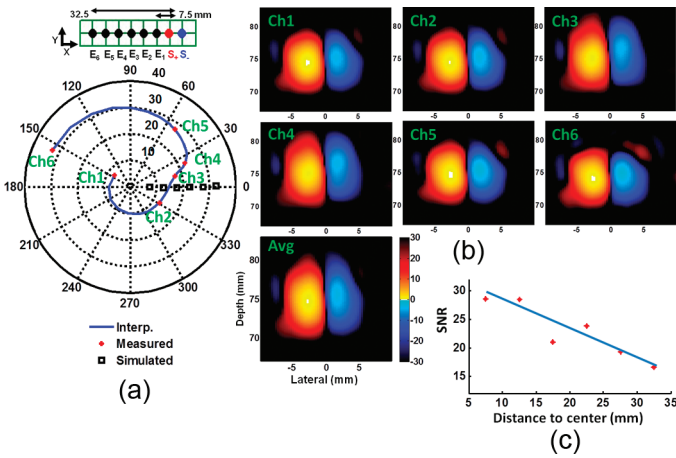


Fig. 7. Distance effect. The phase of the AE signal at the marked position changes with distance from the detector to the center of the dipole. (a) Polar plot of phase shift with distance at the marked position for the measured (red star) and simulated (black square) AE voltage. The maximal absolute value appears in the fourth channel image (Ch4) at the marked position, where the AE voltage has a phase  $0^\circ$  in each channel after adjustment. The interpolated curve (blue) indicates the trend of the phase shift for the measured data. (b) The AE voltage for each channel (1–6) and also the global average are reconstructed, and the phase is adjusted according to the marked position. (c) SNR and sensitivity decays with distance to the dipole. The peak ultrasound pressure at the focus was 530 kPa. The measured peak-to-peak current was 140 mA. The dynamic range is  $[-30, 30]$  dB.

phase of simulated AE voltage at the marked position were  $3.04e-4\angle-0.0268$ ,  $2.96e-4\angle-0.0311$ ,  $2.91e-4\angle-0.0346$ ,  $3.06e-4\angle-0.031$ ,  $3.04e-4\angle-0.024$ ,  $3.07e-4\angle 0.0313$ ,  $3.02e-4\angle-0.0332$ ,  $2.99e-4\angle-0.0176$  [black squares in Fig. 8(a)]. Therefore, the UCSDI is insensitive to the angle between the detector and the dipole. The reconstructed 4-D images from different angles were averaged to enhance the imaging quality. In Fig. 8(b), if the peak value in the bottom left region is selected as the noise, the SNR of the eight channels are, respectively, 25.7, 25.8, 23.9, 23.8, 27.4, 27.1, 28, and 26.2 dB, whereas the SNR of the averaged data is about 26.5 dB.

#### IV. DISCUSSION

Because the correlation between the ultrasound pulse and the inner product of the dipole electric field with the lead field of detector is affected by the high-frequency pulse and low-frequency injected current, it is difficult to directly extract the polarity of the dipole from the raw data. However, when the AE signal is shifted to baseband, both the polarity and envelope of the current density can be obtained at the same time. The correlation makes the shift frequency slightly lower than the center frequency of the detected AE signal. The shift frequency can be optimized by making the area of anodes and cathodes large and uniform. The AE signal encodes the gradient of the dipole's electric field, making the base-banded AE signal positive at the anode and negative at the cathode.

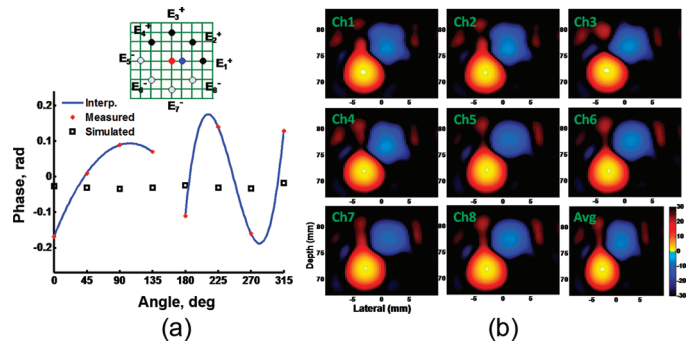


Fig. 8. Angle effect. The phase of the AE voltage at the marked position changes with the angle between the recording electrode and the dipole. The maximal value appears in the fourth channel, and its position is selected as the reference position. The eight channels are synchronized and co-registered by adjusting the phases at the marked position to zero. (a) Phase shift with angle of the measured and simulated AE voltage at the marked position. Channels 1–4 were connected to the positive inputs of the differential amplifiers with negative inputs connected to ground. Channels 5–8 are connected to the negative inputs of the differential amplifiers with positive inputs connected to ground. (b) The AE voltage of each channel (1–8) and averaged data are reconstructed individually. The dynamic range is  $[-30, 30]$  dB.

Each recording electrode detects the AE signal and, after scanning of the ultrasound, produces a 4-D UCSDI. The reconstructed AE voltage from multiple recording electrodes provides complementary information for the analysis of current deep inside tissues. If more recording electrodes are applied, the accuracy and spatial resolution can be improved by averaging over the adjusted data, but this requires channel coregistration. In the experiment, the strongest pixel is chosen as the marked position for synchronizing all the detectors by ensuring the correct phase at the reference position.

The starting phase of the AE A-line is difficult to determine. It can be resolved as the phase of the marked position closely related to the injected current. If the maximal AE voltage at the reference position is detected when the injected current reaches maximum with phase 0, the starting phase is 0 or  $2n\pi$  ( $n$  is integer). On the other hand, when the maximal value occurs at the minimum current with phase  $\pi$ , the starting phase of that reference position deviates by  $\pi$ . In this way, after the phase of the reference position in each channel is adjusted, each A-line in each channel adjusts the phase according to the marked position.

The acquisition speed is limited by the mechanical scanning of the 1-MHz transducer. In theory, UCSDI can be performed as fast as or even faster than traditional pulse-echo ultrasound. Because it only depends on one-way travel of the acoustic pulse, UCSDI might be able to achieve twice the frame rate of a typical ultrasound system. Because clinical 3-D scanners with electronic beam steering can acquire volume images at  $\sim 50$  Hz frame rate, we envision a future clinical system that potentially captures current density images at 100 Hz, which might provide valuable feedback during treatment for cardiac and neural disorders. Moreover, because one detector can ef-

fectively produce 4-D UCSDI images, this technique could dramatically reduce the number of contact points (i.e., electrodes) usually required for electric mapping.

## V. CONCLUSION

Four-dimensional UCSDI of a time-varying electric dipole in saline was presented using as few as one distant electrode and ground. Accurate reconstruction of the current source densities using 4-D UCSDI was demonstrated using simulations combined with bench-top experiments. The detected AE signal is related to the inner product of the lead field of the detector and the dipole field of the injected current. The correlation/convolution between the ultrasound pulse and lead fields effectively shifts the center frequency of the AE signal to a slightly lower frequency. The current direction and amplitude are encoded in the phase and amplitude of the AE signal. The AE signal is sensitive to the distance between the detector and the dipole, but less sensitive to the angle. Small cardiac and neural signals may further require multiple electrodes for averaging to enhance SNR. Hybrid imaging with UCSDI potentially provides real-time 4-D images of current flow (UCSDI) combined with anatomy (co-registered conventional ultrasound) and standard electrophysiology to facilitate and enhance corrective procedures for cardiac and neural abnormalities.

## REFERENCES

- [1] Y. Zhang, W. Drongelen, M. Kohrman, and B. He, "Three dimensional brain current source reconstruction from intra-cranial ECoG recordings," *Neuroimage*, vol. 42, no. 2, pp. 683–695, 2008.
- [2] D. Lai, C. Liu, M. D. Eggen, P. A. Iaizzo, and B. He, "Equivalent moving dipole localization of cardiac ectopic activity in a swine model during pacing," *IEEE Trans. Inf. Technol. Biomed.*, vol. 14, no. 6, pp. 1318–1326, 2010.
- [3] R. D. Pascual-Marqui, M. Esslen, K. Kochi, and D. Lehmann, "Functional imaging with low resolution brain electromagnetic tomography (LORETA): A review," *Meth. Find. Exp. Clin.*, vol. 24, suppl. C, pp. 91–95, 2002.
- [4] Z.-H. Wang, P. Ingram, R. Olafsson, Q. Li, and R. S. Witte, "Detection of multiple electrical sources in tissue using ultrasound current source density imaging," *Proc. SPIE*, vol. 7629, art. no. 76290H, 2010.
- [5] Q. Li, R. Olafsson, P. Ingram, Z.-H. Wang, and R. S. Witte, "Measuring the acoustoelectric interaction constant using ultrasound current source density imaging," *Phys. Med. Biol.*, vol. 57, no. 19, pp. 5929–5941, 2012.
- [6] R. Olafsson, R. S. Witte, S. W. Huang, and M. O'Donnell, "Ultrasound current source density imaging," *IEEE Trans. Biomed. Eng.*, vol. 55, no. 7, pp. 1840–1848, 2008.
- [7] Z.-H. Wang, R. Olafsson, P. Ingram, Q. Li, and R. S. Witte, "Multichannel ultrasound current source density imaging of a 3-D dipole field," in *IEEE Ultrasonics Symp.*, 2010, pp. 253–256.

- [8] Z.-H. Wang, R. Olafsson, P. Ingram, Q. Li, Y. Qin, and R. S. Witte, "Four-dimensional ultrasound current source density imaging of a dipole field," *Appl. Phys. Lett.*, vol. 99, no. 11, art. no. 113701, 2011.
- [9] H. Zhang and L. V. Wang, "Acousto-electric tomography," *Proc. SPIE*, vol. 5320, pp. 145–149, 2004.
- [10] R. Olafsson, R. S. Witte, and M. O'Donnell, "Detection of electrical current in a live rabbit heart using ultrasound," in *IEEE Ultrasonics Symp.*, 2007, pp. 989–992.
- [11] R. Olafsson, R. S. Witte, K. Kim, S. Ashkenazi, and M. O'Donnell, "Electric current mapping using the acousto-electric effect," *Proc. SPIE*, vol. 6147, art. no. 61470O, 2006.
- [12] Z.-H. Wang, P. Ingram, R. Olafsson, C. L. Greenlee, R. A. Norwood, and R. S. Witte, "Design considerations and performance of MEMS acoustoelectric ultrasound detector," *IEEE Trans. Ultrason. Ferroelectr. Freq. Control*, vol. 60, no. 9, pp. 1906–1916, 2013.
- [13] R.-H. Yang, X. Li, J. Liu, and B. He, "3D current source density imaging based on the acoustoelectric effect: a simulation study using unipolar pulses," *Phys. Med. Biol.*, vol. 56, no. 13, pp. 3825–3842, 2011.
- [14] R. Olafsson, R. S. Witte, C.-X. Jia, S. W. Huang, K. Kim, and M. O'Donnell, "Cardiac activation mapping using ultrasound current source density imaging (UCSDI)," *IEEE Trans. Ultrason. Ferroelectr. Freq. Control*, vol. 56, no. 3, pp. 565–574, 2009.
- [15] R. Olafsson, R. S. Witte, S. W. Huang, and M. O'Donnell, "Measurement of a 2D electric dipole field using the acousto-electric effect," *Proc. SPIE*, vol. 6513, art. no. 65130S, 2007.
- [16] W. H. Hayt, J. E. Kemmerly, and S. M. Durbin, *Engineering Circuit Analysis*. New York, NY: McGraw-Hill, 2006, pp. 122–123.
- [17] J. Malmivuo and R. Plonsey, *Bioelectromagnetism: Principles and Applications of Bioelectric and Biomagnetic Fields*. New York, NY: Oxford University Press, 1995, pp. 201–210.



**Zhaohui Wang** (M'10) received his B.S. degree in electronics in 1993 from Shandong University, China; his M.E. degree in circuits and systems in 2002 from the University of Science and Technology of China; his M.S. degree in biomedical engineering in 2005 from University of Toledo, Toledo, OH; his M.S. degree in mechanical engineering in 2008 from the University of Arizona; and his Ph.D. degree in electrical and computer engineering in 2011 from the University of Arizona. He is now a Postdoctoral Fellow at the University of Pittsburgh, Pittsburgh, PA. His current research includes the acoustoelectric effect and photoacoustic imaging.



**Russell Witte** received the B.S. degree in physics with honors from the University of Arizona, Tucson, AZ, in 1993, and the Ph.D. degree in bioengineering from Arizona State University, Tempe, AZ, in 2002. His graduate work exploited chronic, implantable microelectrode arrays to characterize sensory coding, learning, and cortical plasticity in the brain. He then moved to Ann Arbor and the University of Michigan, where he developed noninvasive imaging techniques to explore the neuromuscular and nervous systems. While at the Biomedical Ultrasound Laboratory, he helped devise several methods for enhancing image contrast using ultrasound combined with other forms of energy. He is now Associate Professor of Medical Imaging, Optical Sciences, and Biomedical Engineering at the University of Arizona. His laboratory currently develops novel techniques that integrate light, sound, and electricity for medical imaging. His research potentially impacts applications ranging from epilepsy and arrhythmia to cancer.